Article

Zircon U-Pb Ages of the Granitoids in Shanxi and Its Significance for Tectonic Evolution of North China Craton in Mesozoic

Fuhui Qi [1,2], Pengpeng Li [3] and Chao Liu [4,*]

[1] Shanxi Coal Geological Investigation and Research Institute Co., Ltd., Taiyuan 030024, China; qifuhui01@163.com

[2] Technological Innovation Centre for Comprehensive Exploration on Coal Stratum Minerals in Shanxi Province, Taiyuan 030024, China

[3] Coalbed Methane Exploration and Development Branch, PetroChina Huabei Oilfield Company, Jincheng 048000, China; ppengli2024@163.com

[4] College of Mining Engineering, Taiyuan University of Technology, Taiyuan 030024, China

* Correspondence: liuchao06@tyut.edu.cn

Abstract: Mesozoic granitoid formations offer crucial insights into the tectonic history of the North China Craton. New zircon U-Pb ages of two Mesozoic granitoids in the Huai'an terrane yield ages of 226.4 ± 1.1 Ma for the Yihe (YH) granite and 156.3 ± 2.9 Ma for the Zhujiagou (ZJG) granodiorite. The negative Nb, Ta, and Ti anomalies; high Nb/Ta ratios (20.4 to 24.1); high $(La/Yb)_N$ (30–84); low initial $^{87}Sr/^{86}Sr$ ratios (0.707725–0.708188); and negative $\varepsilon_{Nd}(t)$ values of the Yihe complex suggest that it originated from the partial melting of the lower crust and lithospheric mantle. However, the geochemical and Sr-Nd isotopic results of the ZJG granodiorite are characterized by I-type granites: $Na_2O + K_2O$ values of 7.27 to 7.94 wt%, negative Nb anomalies, positive Pb anomalies, higher initial $^{87}Sr/^{86}Sr$ ratios (0.710979–0.714841), and much lower $\varepsilon_{Nd}(t)$ values (-27.1 to -30.1). The Late Jurassic Zhujiagou complex was derived from partial melting of a thickened low crust, and during the Late Triassic, magmatic rocks were formed under a post-collisional extensional regime. Multiple upwellings of the asthenosphere facilitated the mixing of magmas derived from partial melting of the lithospheric mantle and lower crust. These mixed magmas then ascended to the upper crust after undergoing fractional crystallization, leading to the formation of the YH complex. In the Late Jurassic, the tectonic regime of the NCC shifted from compression to extension. The Late Jurassic intrusion identified in this study developed within a compressional setting linked to the subduction of the Paleo-Pacific Ocean.

Keywords: Mesozoic granitoids; Huai'an terrane; North China Craton; tectonic transformation

1. Introduction

The North China Craton (NCC, Figure 1a), one of the world's oldest cratons with continental rocks dating back ≥ 3.8 billion years [1], plays a crucial role in understanding the evolution of the Paleo-Asian Ocean (PAO) and Paleo-Pacific Ocean [2–6]. According to Zonenshain et al. (1990) [7], the Paleo-Asian Ocean (PAO) closed in the Late Paleozoic, which coincided with the formation of the Central Asian Orogenic Belt [4,8]. Throughout the Mesozoic, the Paleo-Pacific Ocean subducted towards the NWW to NNW beneath the North China Craton, leading to the formation of significant magma bodies [5,9–12]. Despite these complex processes leading to the inversion of the tectonic regime in the North China Craton, the precise timing of this transition remains unclear [4,5]. Li et al. [13] proposed that the Yanshan Movement commenced at 168 Ma, indicating that the extensional tectonic regime of the NCC has changed to a compressional tectonic regime since the Jurassic. Additionally, the tectonic regime transitioned from compressional to extensional at approximately 130 Ma [13]. Zhai et al. [14] proposed that the extensional regime in

the North China Craton began during the Late Jurassic to Early Cretaceous [15,16]. Fan et al. [17] hold the view that the tectonic regime conversion took place during the middle of Mesozoic [18]. In contrast, Shao et al. [19] suggested that the NNE strike Late Mesozoic tectonic-magma belts in the NCC display different tectonic units of the Paleo-Asian Ocean domain, indicating that the conversion of the tectonic regime started in the Late Mesozoic. In addition to multi-staged tectonic events, the NCC has become unstable and fertile, and widely distributed magmatism has been generated in the eastern parts of the NCC [20–22]. The literature has increasingly indicated that the western and central parts of the NCC also have responded to the above-mentioned lithospheric destruction [6,22–24], but the research has been lacking so far as there have only been a few magmatic events.
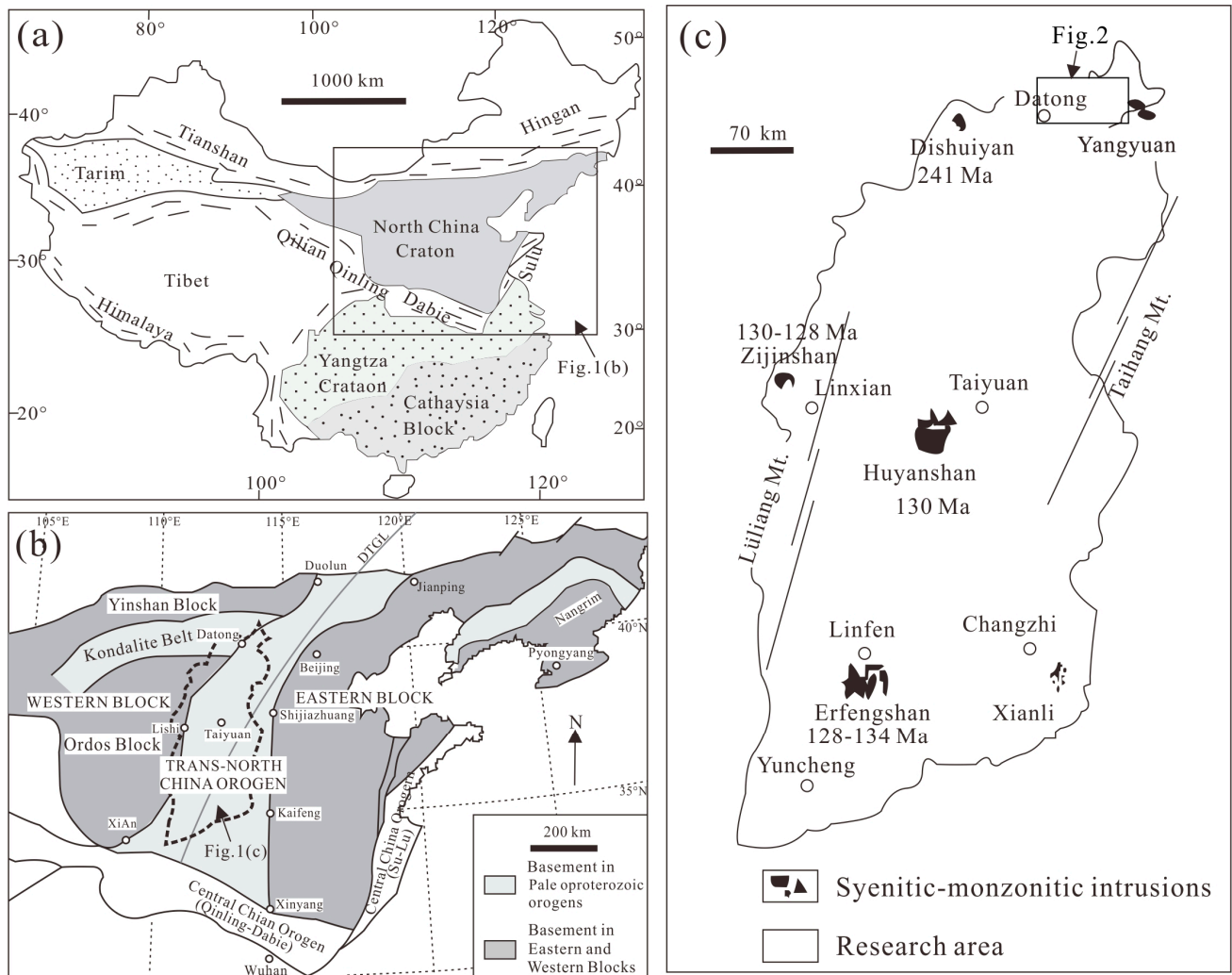
Figure 1. (**a**): Location map showing the tectonic setting of the North China Craton (modified after [20]), (**b**): Simplified geological map of the tectonic subdivision of the North China Craton and location of Shanxi Province, (**c**): The outline of Shanxi Province and the distribution of alkaline intrusive rocks, the rectangle shows the position of Figure 2 (DTGL: Daxinganling-Taihang gravity lineament, modified after [25]).
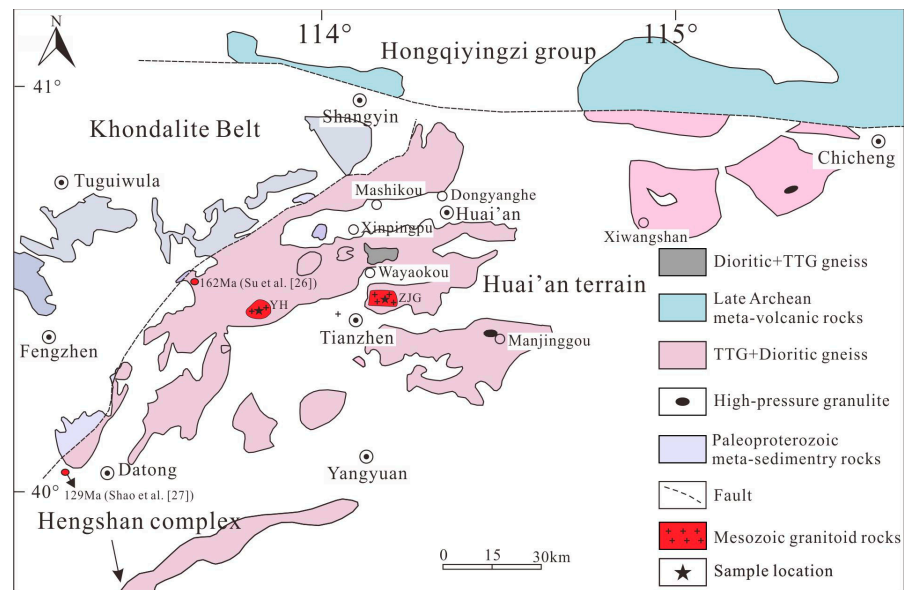
Figure 2. Simplified geological map of the Huai'an complex and sample sites of this study. The Yihe granite–diorite complex is represented by sample YH and the Zhujiagou complex by sample ZJG. The age of Mesozoic granitoid rocks are cited by Su et al. [26] and Shao et al. [27].

The Huai'an terrane is located in the central region of the NCC [28]. The Mesozoic magmatic rocks of the Huai'an terrane have rarely been mentioned in previous research; for example, Su et al. [26] reported a Mesozoic diabase dyke, but they did not provide any detailed information. This study presents new zircon U-Pb geochronological and geochemical data on the Mesozoic granitoids in the Huai'an terrane, which is tectonically located in the central part of the NCC, to provide new evidence for the evolution of the NCC.

2. Geological Setting and Petrography

The Trans-North China Orogen (TNCO) resulted from the continent–continent collision between the Western and Eastern blocks around 1.85 Ga (Figure 1b, [29,30]). The Western Block consists of the Yinshan Block, Ordos Block, and the Khondalite Belt situated between them. The Yinshan Block is primarily composed of greenstone belts, tonalite–trondhjemite–granodiorite (TTG) complexes, sanukitoid plutons, and granulite–charnockite formations [31,32]. The Khondalite Belt comprises graphite-bearing sillimanite–garnet gneiss, garnet quartzite, felsic paragneiss, calc-silicate rocks, and marble. These rocks originally developed at a stable continental margin before becoming part of the collision between the Yinshan and Ordos blocks approximately 1.95 Ga [33,34]. Subsequent to the collision between the Western and Eastern blocks along the Trans-North China Orogen [25], the NCC has become a coherent, largely stable, and long-lived craton. Only rare and minor magmatic activity affected the NCC during the Mesoproterozoic to Early Paleozoic [20]. During the Late Paleozoic, the North China Craton predominantly experienced the subduction and eventual closure of the Paleo-Asian Ocean, followed by the emplacement of Late Permian to Early Triassic syn-collision granitoids along its northern margin [20,35,36].

The Huai'an terrane is situated in the central-north segment of the TNCO, west of the NE-trending Daxing'anling–Taihangshan Gravity Lineament (DTGL, Figure 1b), which is considered to be a major lithosphere/terrane boundary [37]. The terrane consists of tonalitic, trondhjemitic, and granodioritic gneisses (TTG gneisses); high-pressure (HP) granulites; charnockites; K-feldspar granite; and granite gneiss [38,39]. The TTG gneiss, which formed around 2.5 Ga through the partial melting of subducted oceanic crust, contributed to significant crustal growth. This gneiss later experienced granulite facies metamorphism between 1.85 and 1.8 Ga [38]. The HP granulites are distributed as mafic restates in the TTG

gneiss, and magmatic zircon grains in the HP granulites yielded ages between 2.05 and 2.0 Ga [28], interpreted as the timing of mafic magma emplacement during an extensional event [38]. The metamorphic zircon grains provided two distinct age ranges: 1.95–1.90 Ga and 1.85–1.8 Ga. Zhang et al. (2016) [28] proposed that the high-pressure granulite and retrograde granulite metamorphism of the HP granulites occurred at 1.95–1.90 Ga and 1.85–1.8 Ga, respectively, and they crystallized at 702–749 °C [38]. Mesozoic granitoids complexes have been found in the Huai'an terrane, while there is limited research on these complexes. In this research, two Mesozoic complexes have been investigated: the southwestern Yihe complex and the Zhujiagou complex.

The Yihe complex (YH in Figure 2) covers an area of 10 km² in the southwest of the Huai'an terrane. The primary rock type is granite, accompanied by smaller amounts of granodiorite, monzodiorite, and quartz-diorite. The granite is pale red and has an equigranular texture. It consists of K-feldspar (40%–45%), quartz (25%–30%), plagioclase (8%–10%), biotite (15%), hornblende (3%–5%), and minor magnetite, zircon, and apatite (Figure 3). Mu et al. [40] reported an age range of 240–247 Ma, but their method, results, and uncertainties have not been reported.
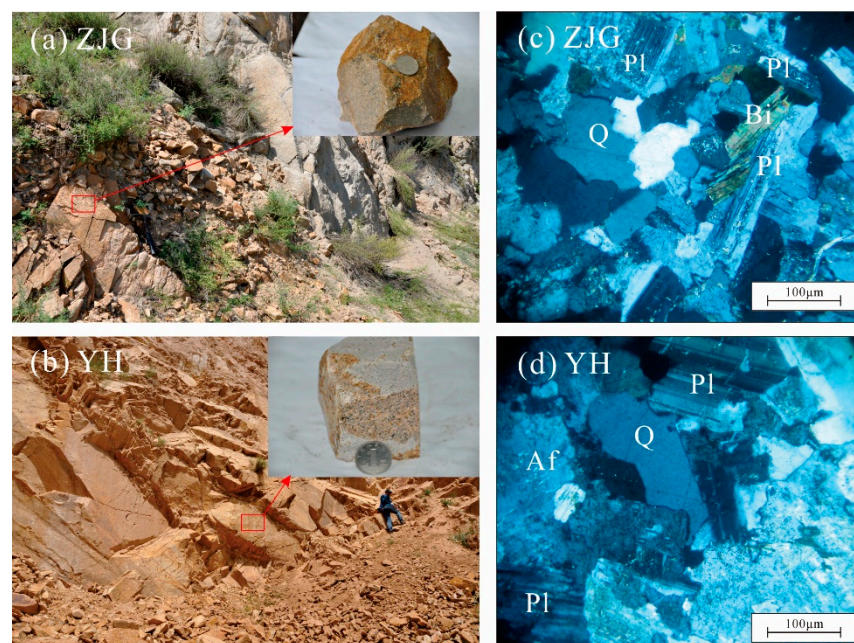
Figure 3. Field photograph of (**a**) ZJG granite–diorite complex; (**c**) ZJG tonalite complex; and Microphotographs (crossed nicols) of (**b**) YH granite–diorite complex; (**d**) YH tonalite complex from Huai'an terrain (Q: quartz; Pl: plagioclase; Bi: biotite; Af: alkali-feldspar).

The Zhujiagou tonalite–granodiorite–porphyry intrusions (ZJG in Figure 2) occur in the southeastern part of the Huai'an terrane where they intrude Neoarchean gneiss, which belongs to the Jining Formation. The complex features several intrusive bodies that extend 800 m in the north–south direction and 600 m in the east–west direction. The primary rock type is granodiorite, with tonalite as a subordinate component; the granodiorite is gray with a phaneritic texture and it contains plagioclase (50%–60%); quartz (22%–25%); K-feldspar (12%–13%); hornblende (3%–5%); and accessory magnetite, zircon, and titanite (Figure 3). The tonalite is grayish-green and porphyritic with plagioclase, which is white-colored with perfect cleavage and albite twins, and has a matrix composed of plagioclase, quartz, amphibole, and accessory minerals, including titanite, apatite, zircon, magnetite, and monazite.

3. Analytical Methods

Whole-rock samples were trimmed to eliminate altered areas. Fresh samples were then fragmented and ground to a 200-mesh powder using an agate mill, preparing them for major and trace element analysis. Major elements were assessed using X-ray fluorescence.

(XRF) spectroscopy was performed with a Philips PW1400 spectrometer at the Institute of Geochemistry, Chinese Academy of Sciences (Guiyang, China). The analytical precision was $\leq 5\%$, as demonstrated by long-term measurements following Chinese national standards GSR-1 and GSR-3. For trace element analysis, 40 mg of whole-rock powder was weighed and dissolved in a mixture of distilled HF and HNO_3 in Teflon screw-cap capsules at 100 °C for 4 days, then dried and treated with HNO_3 at 150 °C for 1 day. The samples were then diluted to 50 mL with 1% HNO_3 prior to analysis. Trace element concentrations were measured using inductively coupled plasma mass spectrometry (ICP-MS), with an analytical uncertainty of less than 5% for values above the detection limits.

An amount of approximately 1 kg of the samples was crushed and pulverized and a Wilfley table was used to concentrate the heavy minerals, which were then further separated using magnetic and heavy liquid techniques. Zircon grains were selected under a binocular microscope and mounted in epoxy resin discs, along with the standard TEMORA 1 (with a $^{206}Pb/^{238}U$ age of 417 Ma, [41]). Cathodoluminescence (CL) and backscattered electron (BSE) techniques were used to select positions for analysis and check the internal textures of zircon crystals. The U-Pb dating was performed using the SHRIMP II instrument at the Beijing SHRIMP center, with a detailed description of the procedure provided by Wan et al. [42]. The data were processed with the SQUID and Isoplot 4 software platforms [43], with age uncertainties reported at a 95% confidence level.

The whole-rock Sr and Nd isotopic compositions were determined at Beijing CreaTech Testing International Co., Ltd. using a Neptune plus MC-ICP-MS instrument. Some detailed preparation and analytical procedures can be found in Yang et al. [44]. The Sr and Nd isotopic ratios were corrected for mass fractionation by normalizing to $^{88}Sr/^{86}Sr = 8.375209$ and $^{146}Nd/^{144}Nd = 0.7219$, respectively.

4. Results

4.1. Zircon U-Pb Ages

Zircon grains from samples of the YH complex are euhedral prisms, light yellow in color. Cathodoluminescence imaging shows extensive oscillatory zoning (Figure 4). These zircons display relatively low uranium content and a Th/U ratio between 0.87 and 1.68 (Table 1); they are generally clear but occasionally feature metamict regions within. Fifteen euhedral zircon grains show relatively high concentrations of U and Th, ranging from 137 to 848 ppm and 119 to 605 ppm, respectively, with U/Th ratios between 0.87 and 1.68 (Table 1). Fifteen spots yield $^{206}Pb/^{238}U$ ages from 230.8 ± 3.1 Ma to 221.5 ± 2.7 Ma, defining a weighted average age of 226.4 ± 1.1 Ma (MSWD = 1.3, Figure 5), which is interpreted as the magmatic crystallization age of the YH complex.

Table 1. Major and element data of the Mesozoic granitoids from Huai'an terrain (YH = Yihe granite–diorite complex. ZJG = Zhujiagou tonalite complex.

Wt%	ZJG-1	ZJG-2	ZJG-3	ZJG-4	ZJG-5	ZJG-6	ZJG-7	YH-1	YH-2	YH-3	YH-4	YH-5
SiO_2	68.35	71.86	69.71	69.11	69.62	69.69	69.14	71.17	73.41	72.63	72.71	72.33
TiO_2	0.49	0.34	0.44	0.35	0.35	0.35	0.36	0.24	0.22	0.23	0.25	0.26
Al_2O_3	13.96	13.37	14.54	14.89	14.81	14.78	14.89	14.09	13.47	13.56	13.48	14.10
T Fe_2O_3	3.60	2.94	2.97	3.04	3.01	2.83	2.97	2.25	2.15	1.63	2.10	2.17
MnO	0.05	0.03	0.03	0.03	0.02	0.02	0.03	0.04	0.01	0.02	0.01	0.00
MgO	0.79	0.78	0.72	0.75	0.71	0.70	0.74	0.52	0.38	0.33	0.32	0.33
CaO	3.55	1.92	2.13	2.03	1.94	1.92	1.93	1.57	0.93	1.54	1.08	0.43

Table 1. *Cont.*

Wt%	ZJG-1	ZJG-2	ZJG-3	ZJG-4	ZJG-5	ZJG-6	ZJG-7	YH-1	YH-2	YH-3	YH-4	YH-5
Na_2O	3.35	2.70	3.21	3.22	3.22	3.17	3.31	3.99	3.96	3.92	3.88	4.04
K_2O	4.59	4.54	4.53	4.48	4.73	4.69	4.76	4.61	4.47	4.65	4.66	4.35
P_2O_5	0.27	0.13	0.16	0.16	0.17	0.17	0.17	0.08	0.08	0.08	0.08	0.08
LOI	0.66	1.13	1.04	1.12	1.05	1.09	1.14	0.98	0.90	1.25	1.01	1.56
TOTAL	99.88	99.74	99.83	99.53	99.89	99.74	99.73	99.54	99.98	99.84	99.59	99.66
$Mg^{\#}$	30	34	32	33	32	33	33	31	26	29	23	23
A/CNK	0.861	1.039	1.033	1.075	1.061	1.071	1.054	0.977	1.031	0.948	1.005	1.161
A/NK	1.452	1.427	1.426	1.466	1.420	1.434	1.403	1.218	1.185	1.180	1.178	1.240
ppm												
Sc	7.19	6.34	24.4	20.9	20.5	21.4	22.4	4.54	4.39	3.78	3.93	4.49
V	65.6	41.5	35.5	35.7	34.3	27.1	32	35.00	37.40	32.50	36.80	40.80
Cr	66.3	10.2	12.7	10.2	9.18	11.4	9.55	14.00	13.00	8.49	9.55	20.30
Co	12	2.78	3.47	3.51	3.43	3.4	3.41	3.22	2.09	1.79	3.04	0.46
Ni	38	2.43	4.68	3.9	4.42	5.97	4.92	4.98	3.27	6.41	1.14	4.93
Rb	92.9	170	177	171	170	174	179	111	114	122	119	106
Sr	1080	355	497	490	475	373	485	1030	908	827	718	618
Y	7.62	16.2	45	16.3	15.6	16.6	15.5	14.20	11.10	12.60	12.70	11.20
Zr	129	219	186	186	184	195	192	316	330	305	303	272
Nb	8.01	14.4	33.34	15.71	15.82	16.16	15.37	21.70	18.70	21.20	21.50	17.40
Cs	0.611	9.5	9.95	9.26	9.26	9.15	9.29	1.32	1.23	1.78	1.40	1.34
Ba	1480	1040	1290	1320	1340	1300	1330	1660	3190	1680	2130	1460
La	47.5	56.8	48.3	58.1	56.7	55.7	57	78.90	38.70	47.00	124	80.80
Ce	88.2	104	84.4	89.4	84.7	88.7	86.1	116.00	72.20	78.90	165	93.40
Pr	9.97	11.3	10.7	9.73	9.35	9.72	9.1	13.30	8.26	9.56	16.9	13.60
Nd	34.5	36	42	33.5	32.1	32.7	30.5	43.20	28.80	33.70	50.50	44.10
Sm	4.75	5.34	8.7	5.4	5.08	5.08	4.75	6.11	4.56	5.32	6.32	6.11
Eu	1.76	0.94	1.411	1.054	1.010	1.036	1.021	1.52	1.25	1.35	1.47	1.52
Gd	3.4	3.71	7.734	4.480	4.241	4.320	4.016	4.41	3.35	3.71	4.50	3.80
Tb	0.367	0.55	1.16	0.58	0.55	0.56	0.53	0.55	0.43	0.52	0.53	0.47
Dy	1.48	2.69	6.32	2.87	2.76	2.86	2.64	2.54	1.88	2.19	2.33	1.98
Ho	0.236	0.5	1.32	0.59	0.58	0.60	0.55	0.43	0.35	0.39	0.41	0.32
Er	0.697	1.54	3.53	1.67	1.59	1.69	1.56	1.24	1.00	1.09	1.18	0.99
Tm	0.087	0.235	0.51	0.24	0.23	0.24	0.22	0.17	0.14	0.15	0.16	0.12
Yb	0.54	1.56	3.43	1.66	1.6	1.68	1.57	1.19	0.94	0.95	1.06	0.80
Lu	0.084	0.238	0.48	0.25	0.24	0.25	0.24	0.16	0.16	0.14	0.15	0.11
Hf	2.8	5.58	5.08	4.93	4.88	4.99	4.89	6.87	7.22	7.23	6.91	6.00
Ta	0.9625	0.8778	2.70	1.15	1.22	1.27	1.18	0.96	0.81	1.04	0.94	0.72
Pb	14.5	15.6	25.62	18.62	19.46	18.48	20.58	25.50	21.70	25.90	21.10	24.80
Th	12.1	13.7	14.9	10.8	13.9	11.5	10.8	21.80	20.50	16.20	16.90	20.60
U	1.21	1.37	2.47	1.41	1.72	1.46	1.38	2.40	1.98	2.90	2.62	3.56
ΣREE	225.41	219.99	209.52	200.73	205.14	199.79	269.72	162.02	184.98	374.50	248.14	225.41

Table 1. *Cont.*

Wt%	ZJG-1	ZJG-2	ZJG-3	ZJG-4	ZJG-5	ZJG-6	ZJG-7	YH-1	YH-2	YH-3	YH-4	YH-5
LREE	214.38	195.51	197.18	188.94	192.94	188.47	259.03	153.77	175.83	364.19	239.53	214.38
HREE	11.02	24.48	12.34	11.79	12.20	11.32	10.69	8.25	9.15	10.31	8.60	11.02
LREE/HREE	19.45	7.99	15.98	16.03	15.82	16.65	24.23	18.64	19.22	35.31	27.84	19.45
La_N/Yb_N	26.12	10.10	25.11	25.42	23.78	26.04	47.56	29.50	35.41	83.91	72.63	26.12
δEu	0.65	0.53	0.66	0.66	0.68	0.71	0.89	0.98	0.93	0.84	0.97	0.65
δCe	1.01	0.91	0.92	0.90	0.93	0.93	0.88	0.99	0.91	0.88	0.69	1.01
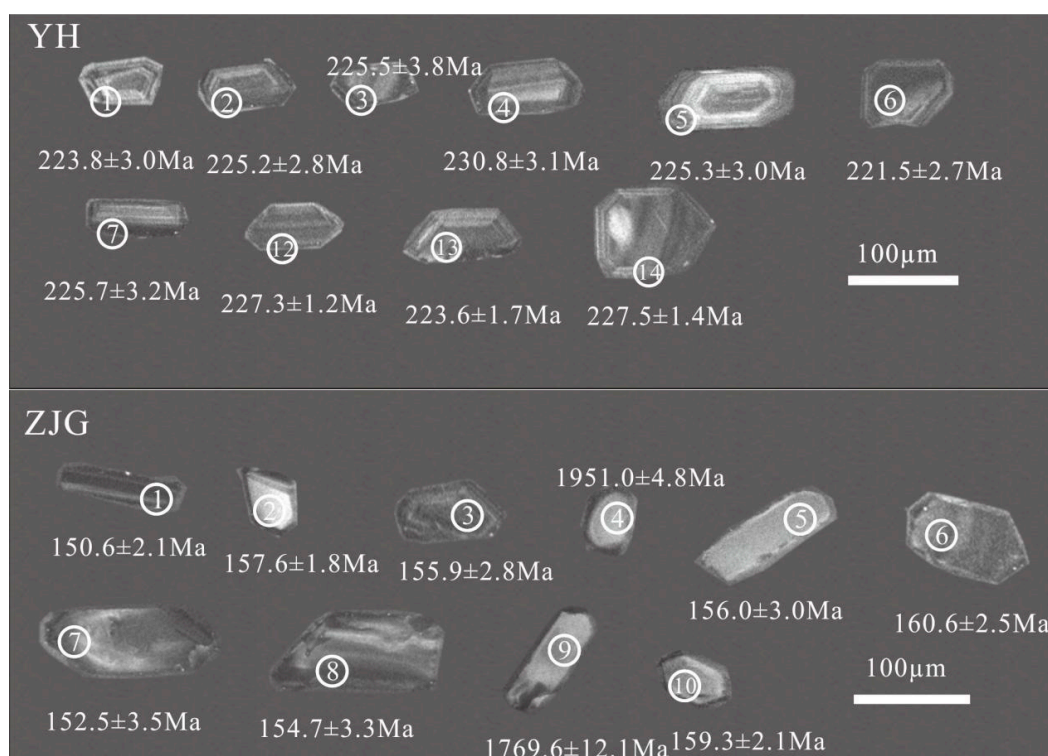
Figure 4. Representative CL images for analyzed zircons of the Mesozoic granitoids from Huai'an terrane.

The zircon crystals extracted from ZJG are generally euhedral, and the zircons measure up to 100 microns in size, with the majority being prismatic and light brown in color. Some zircons feature localized inclusions and metamict areas, potentially indicating older cores; two of them yield discordant analyses with $^{207}Pb/^{206}Pb$ ages of 1951 ± 5 Ma and 1769 ± 12 Ma, probably presenting a xenocrystic origin. These ages are very similar to the metamorphic zircon ages in the basement rocks of the Huai'an terrane, which could have been impacted by Pb loss during the Mesozoic magmatic event. The remaining eight zircons yielded $^{206}Pb/^{238}U$ ages that range from 153 to 161 Ma and define an average $^{206}Pb/^{238}U$ age of 156.3 ± 2.9 Ma (MSWD = 1.8). Only one zircon yielded a younger age of 148.3 ± 1.2 Ma. Thus, we consider the age of 156.3 ± 2.9 Ma as the best estimate for the time of magmatic crystallization of the pluton.
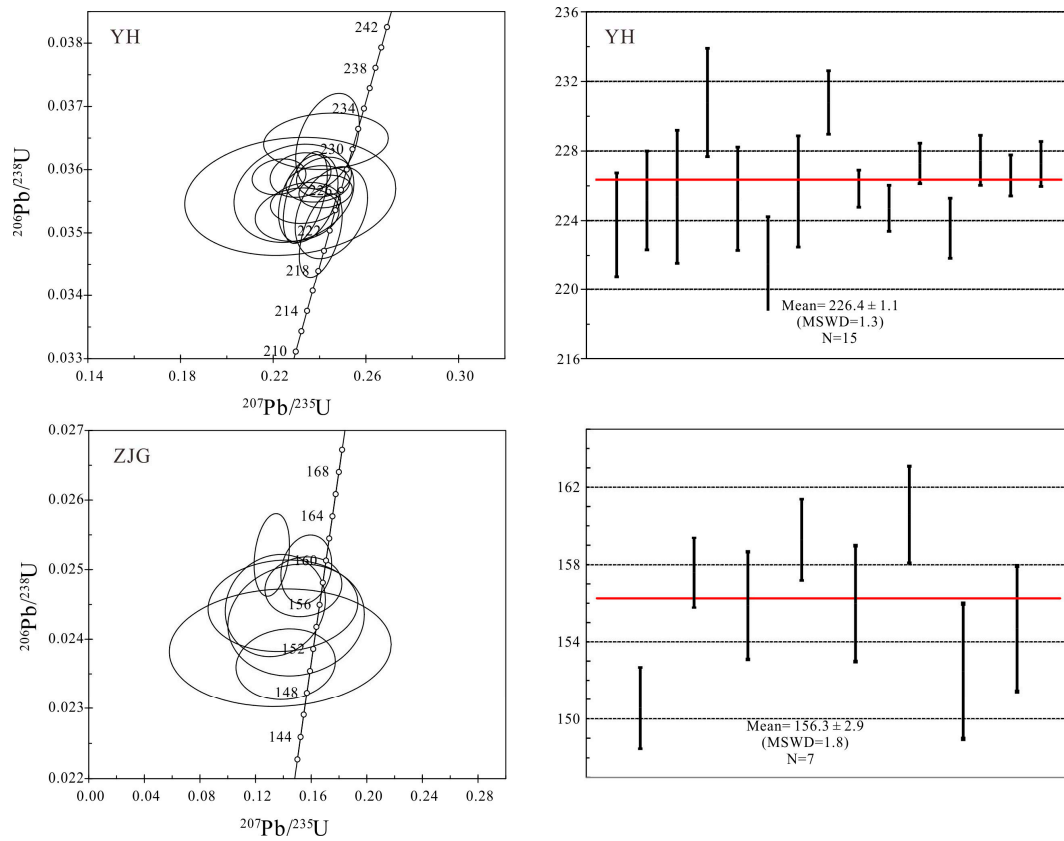
Figure 5. U-Pb concordia diagram of zircons of the Mesozoic granitoids from Huai'an terrane.

4.2. Whole-Rock Compositions of Major and Trace Elements

Table 2 presents the whole-rock major and trace element data for the YH and ZJG complexes, which are also illustrated in Figures 6 and 7.

Table 2. SHRIMP U-Pb data for single zircon grains of Mesozoic granitoids from Huai'an terrain. Pb* indicate the radiogenic Pb.

Spot	U ppm	Th ppm	^{232}Th $/^{238}U$	ppm $^{206}Pb*$	$^{207}Pb*$ $/^{206}Pb*$	±%	$^{207}Pb*$ $/^{235}U$	±%	$^{206}Pb*$ $/^{238}U$	±%	Err Corr	Age	
ZJG-1.1	198	85	0.45	4.18	0.0435	17	0.142	17	0.0236	1.4	0.086	150.6	±2.1
ZJG-2.1	124	77	0.64	2.68	0.0452	12	0.154	12	0.0248	1.1	0.097	157.6	±1.8
ZJG-3.1	71	63	0.91	1.54	0.041	25	0.140	25	0.0245	1.8	0.070	155.9	±2.8
ZJG-4.1	798	465	0.60	242	0.1210	0.30	5.895	0.42	0.3534	0.29	0.684	1951.0	±4.8
ZJG-5.1	113	104	0.96	2.43	0.0398	18	0.134	18	0.0245	2.0	0.111	156.0	±3.0
ZJG-6.1	145	115	0.82	3.19	0.0379	6.2	0.132	6.4	0.0252	1.6	0.244	160.6	±2.5
ZJG-7.1	196	42	0.22	4.54	0.042	38	0.138	38	0.0239	2.3	0.061	152.5	±3.5
ZJG-8.1	77	63	0.84	1.67	0.0446	22	0.149	22	0.0243	2.2	0.100	154.7	± 3.3
ZJG-9.1	197	348	1.83	55.7	0.1082	0.65	4.907	1.5	0.3290	1.3	0.897	1769.6	±12.1
ZJG-10.1	674	80	0.12	14.7	0.0454	7.6	0.157	7.7	0.0250	1.3	0.169	159.3	±2.1
ZJG-11.1	281	189	0.69	5.64	0.0480	5.9	0.154	6.0	0.0233	0.79	0.133	148.1	±1.2
YH-1.1	267	339	1.31	8.18	0.0503	4.0	0.245	4.2	0.0353	1.4	0.323	223.8	±3.0
YH-2.1	472	574	1.26	14.5	0.0480	3.4	0.235	3.6	0.0356	1.3	0.358	225.2	±2.8
YH-3.1	119	137	1.19	3.74	0.0464	13	0.227	13	0.0356	1.7	0.131	225.5	±3.8

Table 2. *Cont.*

Spot	U ppm	Th ppm	$^{232}Th/^{238}U$	ppm $^{206}Pb^*$	$^{207}Pb^*/^{206}Pb^*$	±%	$^{207}Pb^*/^{235}U$	±%	$^{206}Pb^*/^{238}U$	±%	Err Corr	Age	
YH-4.1	244	252	1.07	7.68	0.0484	3.5	0.243	3.7	0.0365	1.4	0.368	230.8	±3.1
YH-5.1	273	230	0.87	8.36	0.0477	2.3	0.234	2.7	0.0356	1.3	0.502	225.3	±3.0
YH-6.1	589	517	0.91	17.8	0.0499	2.2	0.241	2.5	0.0350	1.3	0.493	221.5	±2.7
YH-7.1	238	269	1.16	7.39	0.0466	7.3	0.229	7.5	0.0356	1.4	0.192	225.7	±3.2
YH-8.1	385	511	1.37	12.0	0.0489	3.2	0.242	3.2	0.0359	0.58	0.178	227.3	±1.3
YH-9.1	378	371	1.01	12.0	0.0483	7.3	0.243	7.3	0.0365	0.80	0.110	230.8	±1.8
YH-10.1	605	751	1.28	18.6	0.0494	3.1	0.243	3.1	0.0357	0.48	0.153	225.9	±1.1
YH-11.1	399	559	1.45	12.3	0.0478	4.2	0.234	4.3	0.0355	0.60	0.141	224.7	±1.3
YH-12.1	522	848	1.68	16.2	0.0450	3.4	0.223	3.4	0.0359	0.52	0.150	227.3	±1.2
YH-13.1	218	262	1.25	6.66	0.0473	5.1	0.230	5.2	0.0353	0.79	0.151	223.6	±1.7
YH-14.1	308	341	1.14	9.57	0.0468	3.7	0.232	3.7	0.0359	0.65	0.173	227.5	±1.4
YH-15.1	505	548	1.12	15.6	0.0485	3.8	0.239	3.8	0.0358	0.53	0.139	226.6	±1.2
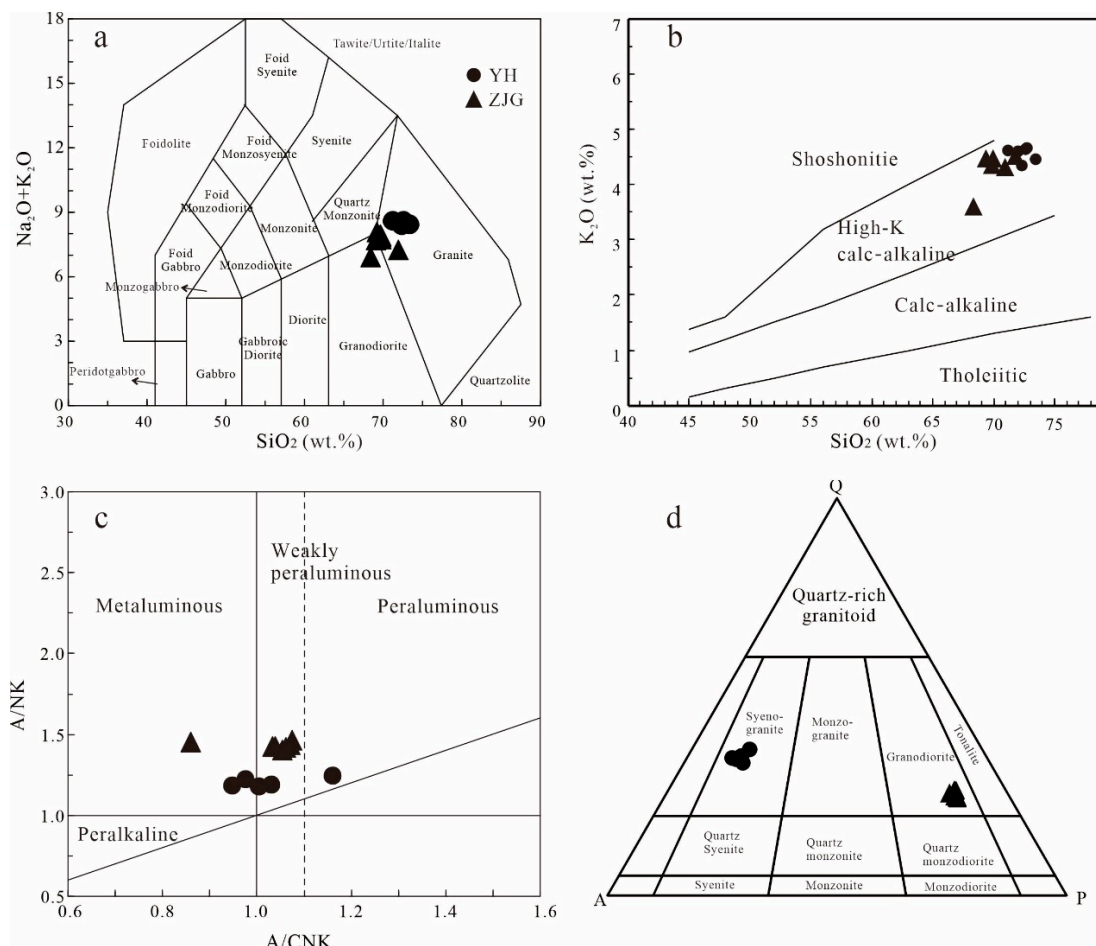
Figure 6. Major element concentrations for the Mesozoic granitoids from Huai'an terrain: (**a**) SiO$_2$ versus total alkali (Na$_2$O + K$_2$O) content diagram [45]; (**b**) K$_2$O versus SiO$_2$ diagram (after [46]); (**c**) A/CNK versus A/NK diagram (A/CNK = molar ratio of Al$_2$O$_3$/(CaO + Na$_2$O + K$_2$O), A/NK = molar ratio of Al$_2$O$_3$/(Na$_2$O + K$_2$O)); (**d**) Q-A-P (quartz-alkali feldspar-plagioclase feldspar) diagram.
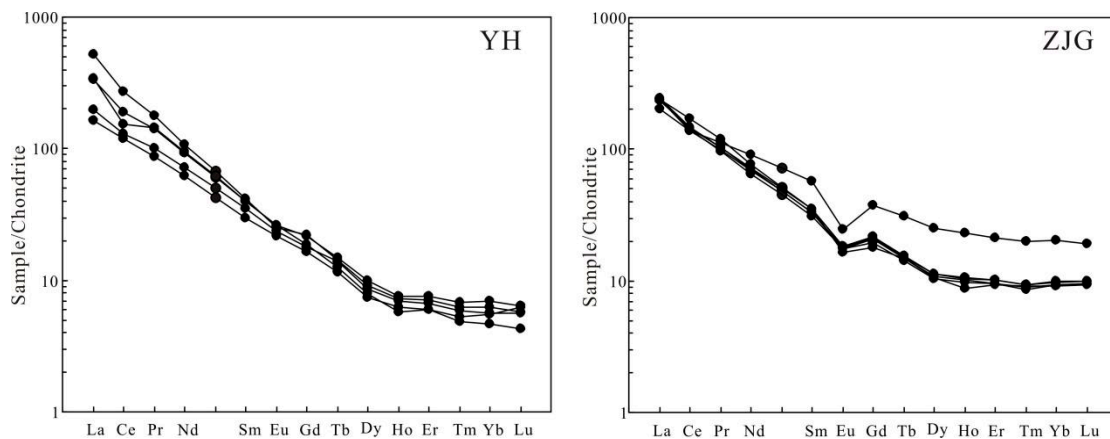
Figure 7. Chondrite-normalized REE patterns of the Mesozoic granitoids from Huai'an terrain. Chondrite values are from [47].

Five YH complex samples show SiO_2 contents ranging from 71 wt% to 73 wt% and total alkali (K_2O + Na_2O) contents between 8 wt% and 9 wt%, plotted in the granite field on the total alkali-versus-silica (TAS) diagram (Figure 6a), a pattern consistent with the observed results (Figure 6d). These samples have a K_2O content of 4.35–4.66 wt% with a K_2O/Na_2O ratio of 1.08–1.20 wt%. In the K_2O-versus-SiO_2 diagram (Figure 6b), all the samples are classified within the high-K calc-alkaline series. The molar ratios of $Al_2O_3/(CaO + Na_2O + K_2O)$ (A/CNK) of YH vary from 0.95 to 1.16, while the ratios of $Al_2O_3/(Na_2O + K_2O)$ (A/NK) range from 1.47 to 1.90. These ratios are plotted along the boundary between the metaluminous and peraluminous fields (Figure 6c). These granite samples exhibit low MgO content, ranging from 0.33 to 0.51 wt%, with $Mg^{\#}$ values varying between 23 and 31 (Table 2).

In chondrite-normalized REE plots (Figure 7), the YH complex shows an elevated total REE content ($\sum$REE = 162–374 ppm) and an enrichment in light rare-earth elements (LREEs) displaying high $(La/Yb)_N$ ratios between 30 and 80, and the rocks also have weakly negative Eu anomalies (Eu/Eu* = 0.84–0.98). In a spidergram normalized to the primitive mantle (Figure 8), the YH complex is enriched in large-ion lithophile elements (e.g., K, Rb, Ba) and shows depletion in high-field-strength elements (HFSEs) like Nb, Ta, P, and Ti. The multi-element normalized spidergram displays negative Nb anomalies and slightly positive Pb anomalies (Figure 8). The negative anomalies in Nb, Ta, and Ti, together with the high Nb/Ta ratios (20.4 to 24.1), imply that rutile is present as a residual phase [31]. The low Yb (0.8–1.1 ppm) and high $(La/Yb)_N$ (30–84) concentrations of HREE and the strong fractionation between LREE and HREE suggest the existence of garnet as a residual phase. The high Sr concentration and the absence of significant negative Eu anomalies suggest that plagioclase is not present as a residual phase.

Compared to the YH complex, the ZJG complex has lower SiO_2 and Na_2O but higher MgO and Al_2O_3 (Figure 9). The ZJG complex has an SiO_2 content of 68.35 to 71.86 wt% and a total alkali content of Na_2O + K_2O ranging from 6.94 to 8.37 wt%, plotted in the granodiorite field in the total alkali-versus-silica (TAS) diagram (Figure 6a), an observation consistent with the results shown in the QAP diagram (Figure 6d). These granodiorite samples have K_2O/Na_2O ratios of 1.07–1.68 and fall within the high-K calc-alkaline series on the K_2O versus SiO_2 diagram (Figure 6b). The A/CNK and A/NK aluminum saturation indices predominantly range from 0.86 to 1.04 and from 1.14 to 1.68, respectively, displaying weakly peraluminous characteristics (Figure 6c). These samples are also characterized by an MgO content ranging from 0.70 to 0.79 wt%, with relatively consistent $Mg^{\#}$ values between 30 and 34 (Table 2).
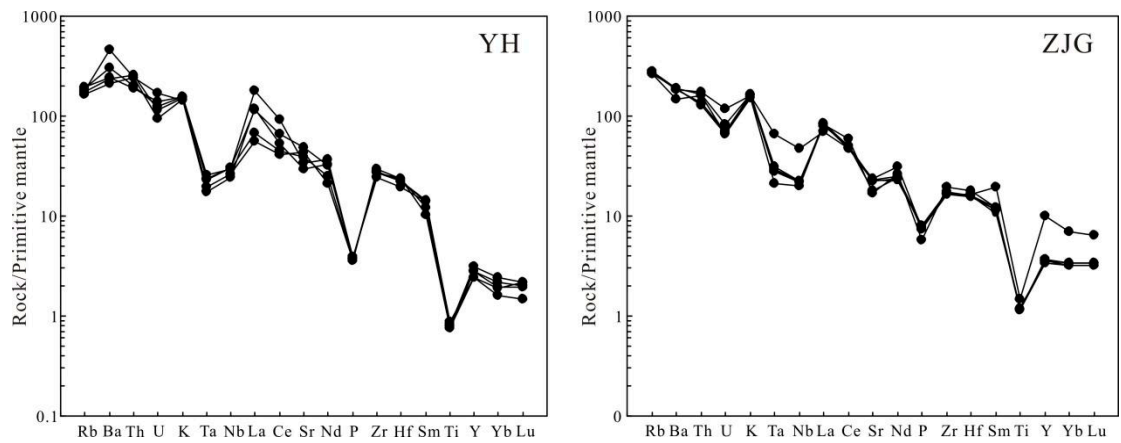
Figure 8. Primitive mantle-normalized trace element patterns of the Mesozoic granitoids from the Huai'an terrain, with primitive mantle values sourced from [47].
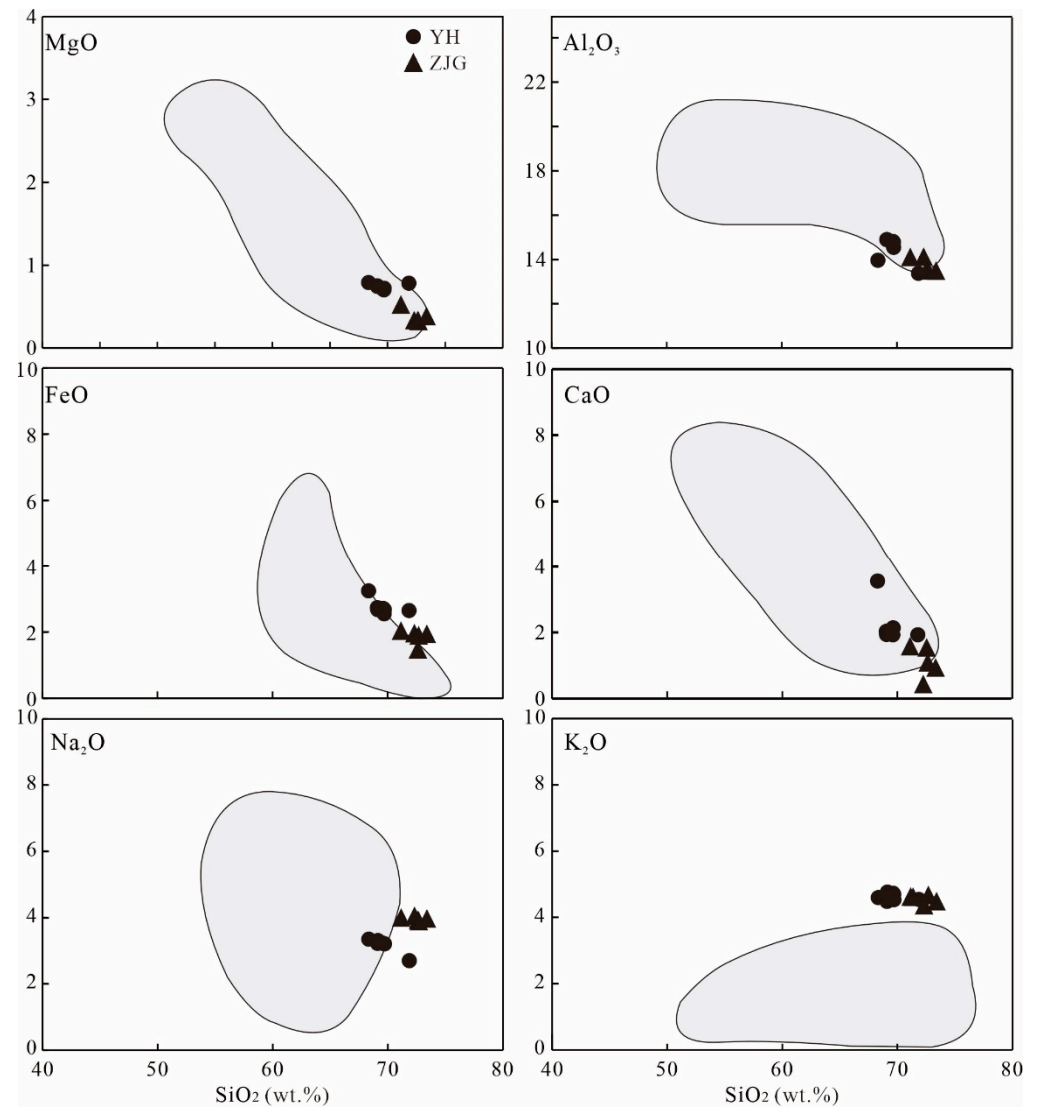
Figure 9. Variations in major element oxides for the Mesozoic granitoids from the Huai'an terrain. The shaded area indicates the compositions of partial melts derived from lower crustal rocks in experimental studies [22,48–50].

These granodiorite samples have a total REE content of 199.79 to 269.72 ppm. In the chondrite-normalized REE diagram, the ZJG complex exhibits enrichment in LREEs while showing a relative depletion in HREEs (LREE/HREE = 19.5–27.1, La_N/Yb_N = 26.1–63.1) and strongly negative Eu anomalies (Eu/Eu* = 0.53–0.71). In a primitive mantle-normalized spidergram (Figure 8), HFSE depletion; enrichment in Ba, Rb, and K; and depletion in U and Ta are displayed. Additionally, they exhibit high Rb (92.9–179 ppm) and Sr (355–1080 ppm) concentrations, with low Y (7.62–16.6 ppm) levels.

4.3. Nd-Sr Isotopes

The whole-rock Nd and Sr isotopic data of granitic rocks from the YH and ZJG complexes are listed in Table 3. The YH complex yields initial $^{143}Nd/^{144}Nd$ ratios of 0.511980 to 0.512039, low initial $^{87}Sr/^{86}Sr$ ratios (0.707725–0.708188), and negative $\varepsilon_{Nd}(t)$ values of −8.7 to −9.9, and the Nd model ages (TDM) range between 1507 Ma and 1352 Ma. The ZJG complex has lower initial $^{143}Nd/^{144}Nd$ ratios (0.510983–0.511128) and higher initial $^{87}Sr/^{86}Sr$ ratios (0.710979–0.714841), as well as much lower $\varepsilon_{Nd}(t)$ values (−27.1 to −30.1), and their TDM are 2650 Ma and 2352 Ma.

Table 3. Sr-Nd isotopic composition of Mesozoic granitoids in Huai'an terrain are calculated using Chondrite Uniform Reservoir (CHUR) values and decay constants of $\lambda_{Rb} = 1.42 \times 10^{-11}$ year^{-1} [51] and $\lambda_{Sm} = 6.54 \times 10^{-12}$ year^{-1} [52].

Sample No.	Rb (ppm)	Sr (ppm)	^{87}Rb/^{86}Sr	^{87}Sr/^{86}Sr	2sigma	ISr	Sm (ppm)	Nd (ppm)	^{147}Sm/^{144}Nd	^{143}Nd/^{144}Nd	2sigma	TDM (Ma)	INd	$f_{Sm/Nd}$	$\varepsilon_{Nd}(0)$	$\varepsilon_{Nd}(t)$
ZJG-1	92.9	1080	0.249	0.714841	0.000009	0.714841	4.75	34.5	0.083	0.511128	0.000002	2352	0.511041	−0.58	−29.4	−27.1
ZJG-2	170	355	0.386	0.710979	0.000007	0.710979	5.34	36	0.090	0.510983	0.000004	2650	0.510889	−0.54	−32.3	−30.1
YH-1	111	1030	0.312	0.707725	0.000007	0.706703	6.11	43.2	0.086	0.511994	0.000004	1374	0.511865	−0.57	−12.6	−9.3
YH-2	114	908	0.363	0.707767	0.000008	0.706577	4.56	28.8	0.096	0.512039	0.000006	1435	0.511894	−0.51	−11.7	−8.7
YH-3	122	827	0.427	0.708188	0.000006	0.706790	5.32	33.7	0.095	0.511980	0.000005	1507	0.511836	−0.51	−12.8	−9.9
YH-5	106	618	0.496	0.707956	0.000006	0.706330	6.11	44.1	0.084	0.511997	0.000008	1352	0.511871	−0.57	−12.5	−9.2

5. Discussion

5.1. Petrogenetic Constraints on the Genesis of the Yihe Complex

The geochemical characteristics of the YH granite include high SiO_2 and Na_2O contents and low MgO, which resemble the major compositions of partial melts produced from lower crustal materials in partial melting experiments (Figure 9; [48,53]). The patterns of Rb, Nb, Ta, P, and Ti depletion, alongside Ba and K enrichment, further suggest that the source of these materials is crustal. In the Th/Hf versus Th and Ba/Nd versus Ba diagrams, these granites predominantly plot along the partial melting trend line, indicating that partial melting was the primary process in their magmatic evolution (Figure 10). Additionally, the absence or weak presence of Eu anomalies in these granites suggests that plagioclase fractionation was not a significant factor in the magma's evolution [22].
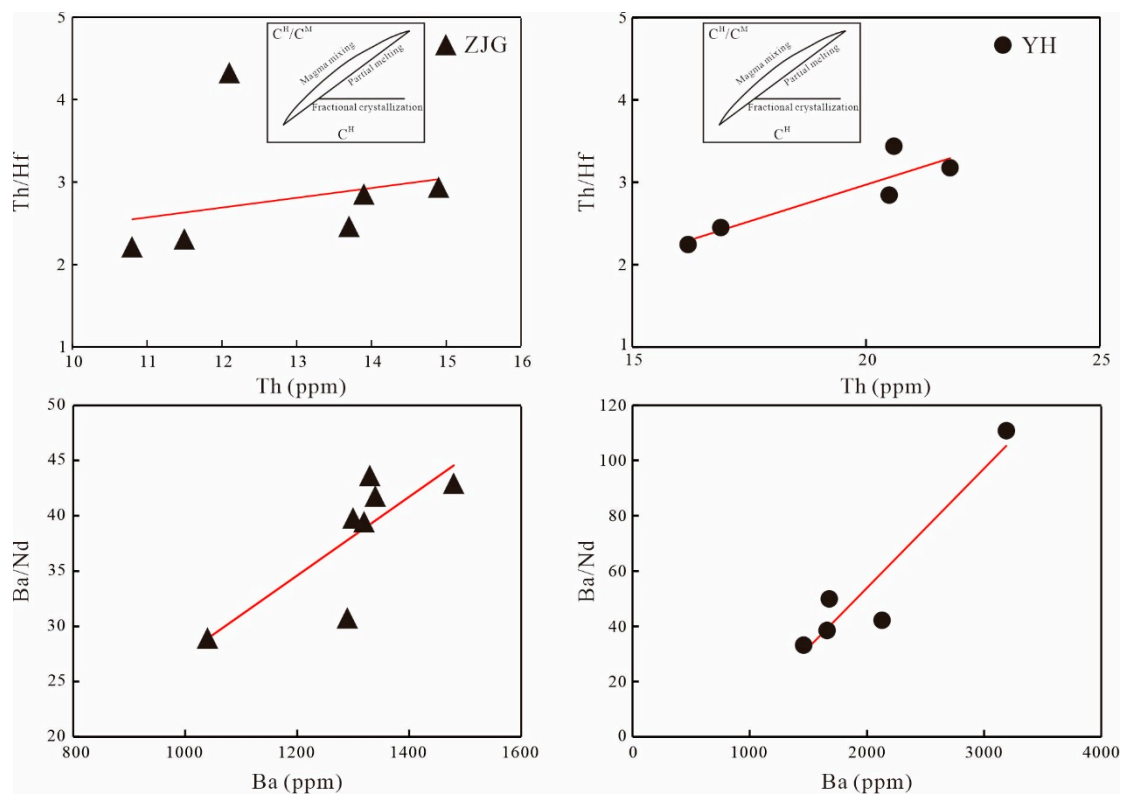
Figure 10. Petrogenetic discrimination diagrams for the Mesozoic granitoids from the Huai'an terrain are presented as Th/Hf versus Th and Ba/Nd versus Ba. Insets depict schematic C^H versus C^H/C^M diagrams (where C^H denotes highly incompatible element concentrations and C^M denotes moderately incompatible element concentrations). The curves represent calculated melt compositions resulting from partial melting, magma mixing, and fractional crystallization (revised [54]).

Nevertheless, the high negative $\varepsilon_{Nd}(t)$ values of the YH complex (-9.9 to -8.7) are markedly different from the much lower values of the NCC lower crust (-35 [22] and its references therein). Thus, the partial melting of the lower crust alone does not account for the parental magmas to the YH quartz monzodiorite. Generally, the magmatic sources of peralkaline plutons are closely associated with an enriched mantle [6,31,55]. The lithologies of YH quartz monzodiorite display the characteristics of being rich in alkali and low in Fe and Mg; these plutons belong to an alkaline–subalkaline series (Figure 8). Based on previous studies of adjacent alkaline intrusions, including the Dishuiyan, Huyanshan, Erfengshan, and Zijinshan complexes, which exhibit similar Sr and Nd isotopic compositions to the YH complex, it is further confirmed that the alkaline magmas in Shanxi Province are derived from both crustal and mantle sources [6,22]. Therefore, we infer that, in addition to crustal materials, the lithospheric mantle may also be a source for the YH complex.

5.2. Petrogenetic Constraints on the Genesis of the Zhujiagou Complex

The geochemistry of the ZJG complex is characterized by high SiO_2 and low P_2O_5, with a negative correlation between SiO_2 and P_2O_5, which are typical features of I-type granites [56]. The ZJG complex belongs to the high-K calc-alkaline series (Figure 6) and has moderate $Na_2O + K_2O$ values (7.27 to 7.94 wt%) and 10000Ga/Al ratios (2.2–2.3) when compared with typical A-type granites (2.6). They also have lower A/CNK values (0.86–1.04) than those of highly felsic, S-type granites (1.1). In primitive mantle-normalized trace element spidergrams (Figure 7), the ZJG complex displays negative Nb anomalies and positive Pb anomalies, which are comparable with I-type granites [57]. In the Th/Hf versus Th and Ba/Nd versus Ba diagrams, these granodiorites predominantly align with the partial melting trend line, indicating that their magmatic evolution was primarily governed by partial melting (Figure 10). The ZJG complex is thus classified as a high-K, calc-alkaline, I-type granite, rather than A- or S-type.

Generally, calc-alkaline I-type granitoids are generated via the partial melting of crustal meta-igneous rocks or the mixture of crustal- and mantle-derived magmas [58]. These ZJG granodiorites are characterized by low MgO content and low $Mg^{\#}$ values (30–34), suggesting that mantle-derived magma plays a minimal role in their petrogenesis. Furthermore, the high initial $^{87}Sr/^{86}Sr$ ratios and negative $\varepsilon_{Nd}(t)$ values (−27 to −35) are comparable to the value of lower lithospheric crust (−35, [22]). In addition, the K/Rb ratios of the ZJG complex range from 220 to 320, matching those of the mature continental crust (100–300, [59]). The inherited zircons have ages consistent with those of the lower crust in the study area, also providing evidence for the lower crustal magma in the petrogenesis. We thus infer that the ZJG complex was generated from the partial melting of the lower crust.

5.3. Geodynamic Implications

Zircon U-Pb dating indicates that the YH complex originated in the Late Triassic, while the ZJG granite dates back to the Late Jurassic. Although the locations of these two complexes are very close, the contrasting ages indicate that they may have been formed under different tectonic settings. The genesis and characteristics of these two complexes provide significant insights into the evolution of the NCC.

5.3.1. Late Triassic YH Complex

It is widely agreed that the Paleo-Asian Ocean (PAO) had already closed by the Middle to Late Triassic [5,20,22,60,61], as also evidenced by the cessation of marine sediment deposition in the eastern section of the Xing-Meng Orogenic Belt during the Early Triassic [62]. After the complete closure of the PAO, the northern NCC began to evolve into a post-collisional or post-orogenic extensional tectonic setting during the Middle to Late Triassic [62,63]. Subsequently, massive magmatic rocks have become widespread along the northern margin of the NCC (Figure 11), such as Fengning gneiss mylonite (237 ± 1 Ma, [64]), Chicheng granite mylonite (234 ± 1 Ma, [64]), Baotou Shadegai calc-alkaline granite (235 ± 3 Ma, [20]), Yaojiazhuang alkalic complex (234 ± 4 to 221 ± 5 Ma, [20]), Sungezhuang alkalic complex (231 ± 2 Ma, [20]), and Dishuiyan monzonite (241.0 ± 2.8 Ma, [22]). These magmatic rocks are distinguished by low initial $^{87}Sr/^{86}Sr$ ratios and negative $\varepsilon_{Nd}(t)$ and $\varepsilon_{Hf}(t)$ values [5,20,22], which suggests that they were produced under the extensional environment associated with the subduction of the Paleo-Asian Ocean plate beneath the NCC. Furthermore, the Late Triassic extension deformation patterns have been suggested to be correlated with the sedimentation in the Helanshan and Zuozishan complexes [20,65]. The Late Triassic YH complex belongs to the alkaline series, indicating it formed in a within-plate setting, an extension environment potentially linked to the closure of the PAO. On the plots of Rb vs. Yb + Nb and Rb vs. Yb + Ta, the YH complex falls within the fields of post-collision granite (Figure 12). Considering the trace element and Sr-Nd isotopic compositions, we suggest that the YH monzonite was formed in a post-collisional extensional regime. The multiple upwellings of asthenosphere promoted the mixing of magmas facilitated the mixing of magmas generated by partial melting of the lithospheric

mantle and lower crust, and then by the magmas mixing upward to the upper crust after fractional crystallization to form the YH complex.
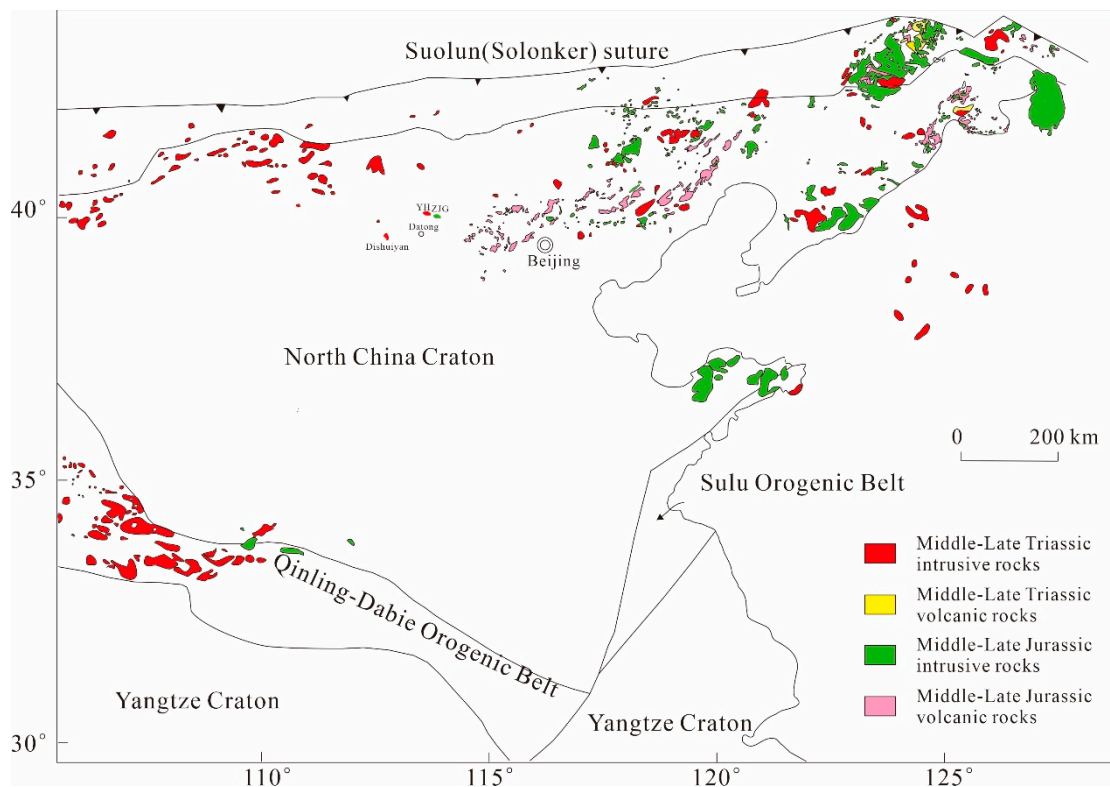
Figure 11. Sketch map illustrating the distribution of the late Triaccic and Jurassic magmatic rocks in the NCC (modified after Zhang et al. [20]).
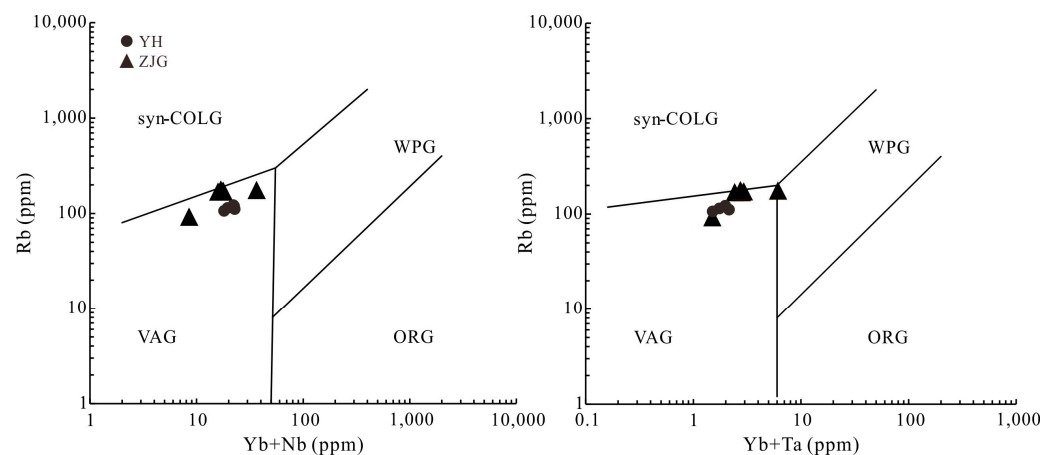
Figure 12. Trace element discrimination diagrams for the ZJG and YH complex [66]. VAG—volcanic arc granites; ORG—ocean ridge granite; WPG—within-plate granites; syn-COLG—syn-collisional granites.

5.3.2. Late Jurassic ZJG Complex

The ZJG complex was emplaced in the Late Jurassic, during which the NCC was affected by far-field effects from the subduction of the Mongol-Okhotsk Ocean to the north, the Paleo-Pacific Ocean to the east, and the Neo-Tethys Ocean to the southwest [67,68]. This resulted in multi-directional contractional deformation, involving lithospheric shortening and thickening [20,69] and the widespread distribution of Late Jurassic magmatic

rocks in the eastern or northeastern parts of the NCC [20,31,69]. Late Jurassic magmatic rocks are predominantly found in eastern, northeastern, and northern regions of the NCC, such as Diaoquan biotite adamellite (154 ± 1 Ma), Tiewadian diorite (153.4 Ma, [70]), Liulengshan complex (153.4 Ma, [70]), and Zhijiadi quartz porphyry (156.0 Ma, [70]), and the volcanic rocks of the Tiaojishan Formation are extensively spread throughout the NCC (156–153 Ma, [71]). These rocks exhibit high contents of $K_2O + Na_2O$, high Sr/Y and La_N/Yb_N ratios, a depletion of high-field-strength elements, low to moderate initial $^{87}Sr/^{88}Sr$ ratios, and negative $\varepsilon_{Nd}(t)$ values [5,20]. These characteristics suggest that the rocks originated from the partial melting of a thickened lower crust [20]. The ZJG complex displays a geochemical affinity to I-type granites and has similar geochemical characteristics to those of coeval granitoids of the eastern NCC [5,6,31,44,72], which formed in a compression environment associated with the subduction of the Paleo-Pacific Plate. However, research indicates that the geodynamic context of the Middle–Late-Jurassic igneous rocks in the NCC is connected to the subduction of the Mongol-Okhotsk Ocean [69,73]. Guo et al. [74] suggested that the igneous rocks from the Yanshan fold and thrust belt (YFTB) are influenced little by the subduction of the Mongol-Okhotsk Ocean, noting that the distribution, composition, and formation of Jurassic volcanic rocks in the YFTB differ from those in the Great Xing'an Range. Furthermore, the contemporaneous igneous rocks in the Erguna–Xing'an massif, primarily A-type granites, were produced in an extensional setting associated with the subduction of the Mongol-Okhotsk Ocean [75,76]. In this study, the formation of the ZJG complex is attributed to the Paleo-Pacific Plate rather than the Mongol-Okhotsk Ocean. In addition, on the plots of Rb vs. Yb + Nb and Rb vs. Yb + Ta, the ZJG complex is categorized as volcanic arc granite (VAG) (Figure 12). It is worth noting that the sedimentological and structural evidence demonstrated a compression setting during the Middle–Late Jurassic [20,77]. Zhao et al. [72] proposed that Middle–Late-Jurassic deformations were predominantly shaped by a contractional environment influenced by various tectonic regimes. The large-scale E-W- or NE-SW-trending thrust faults and folds of the Middle–Late Jurassic developed along the northern margin of the NCC, aligning approximately parallel to the Paleo-Pacific subduction zone [20]. Therefore, we determine that the Late Jurassic intrusion identified in this study originated in a compression regime associated with the subduction of the Paleo-Pacific Ocean.

6. Conclusions

Based on the geochemical and geochronological data of Mesozoic granitoids in the Huai'an terrane, the following conclusions can be drawn:

(1) There were two episodes of magmatism in the Huai'an terrane, namely, the Middle Triassic and Late Jurassic, indicated by U-Pb ages of 226.4 ± 1.1 Ma for the Yihe granite and 156.3 ± 2.9 Ma for the Zhujiagou granodiorite.

(2) The trace element and Sr-Nd isotopic analysis results reveal that the Yihe complex originated from the partial melting of the lower crust and the enriched lithospheric mantle, while the ZJG complex was produced from the thickened lower crust.

(3) The YH and ZJG complexes were generated under two different geodynamic settings: the YH complex developed in a post-collisional extensional regime associated with the Paleo-Asian oceanic plate beneath the NCC, while the Late Jurassic ZJG complex was produced under a compression regime associated with the subduction of the Paleo-Pacific Ocean.

Author Contributions: Conceptualization, methodology, investigation, F.Q., P.L. and C.L.; data curation, F.Q.; writing—original draft preparation, F.Q. and C.L.; writing—review and editing, P.L. and C.L.; supervision, C.L.; funding acquisition, C.L. All authors have read and agreed to the published version of the manuscript.

Data Availability Statement: The data are provided in the article.

Conflicts of Interest: The Author Fuhui Qi was employed by the Shanxi Coal Geological Investigation and Research Institute CO and the author Pengpeng Li was employed by the Coalbed Methane Exploration and Development Branch, PetroChina Huabei Oilfield Company. The remaining authors declare that the research was conducted in the absence of any commercial or financial relationships that could be construed as a potential conflict of interest.

References

1. Liu, D.Y.; Wilde, S.A.; Wan, Y.S.; Wu, J.A.; Zhou, H.Y.; Dong, C.Y.; Yin, X.Y. New U-Pb and Hf isotopic data confirm Anshan as the oldest preserved segment of the North China Craton. *Am. J. Sci.* **2008**, *308*, 200–231. [CrossRef]
2. Wilde, S.A. Final amalgamation of the Central Asian Orogenic Belt in NE China: Paleo-Asian Ocean closure versus Paleo-Pacific plate subduction—A review of the evidence. *Tectonophysics* **2015**, *662*, 345–362. [CrossRef]
3. Safonova, I.; Biske, G.; Romer, R.L.; Seltmann, R.; Simonov, V.; Maruyama, S. Middle Paleozoic mafic magmatism and ocean plate stratigraphy of the South Tianshan, Kyrgyzstan. *Gondwana Res.* **2016**, *30*, 236–256. [CrossRef]
4. Liu, Q.; Zhao, G.C.; Han, Y.G.; Eizenhöfer, P.R.; Zhu, Y.L.; Hou, W.Z.; Zhang, X.R. Timing of the final closure of the Paleo-Asian Ocean in the Alxa Terrane: Constraints from geochronology and geochemistry of Late Carboniferous to Permian gabbros and diorites. *Lithos* **2017**, *274–275*, 19–30. [CrossRef]
5. Ma, X.H.; Zhu, W.P.; Zhou, Z.H.; Qiao, S.L. Transformation from Paleo-Asian Ocean closure to Paleo-Pacific subduction: New constraints from granitoids in the eastern Jilin-Heilongjiang Belt, NE China. *J. Asian Earth Sci.* **2017**, *144*, 261–286. [CrossRef]
6. Wang, K.; Li, Y.L.; Xiao, W.J.; Zheng, J.P.; Wang, C.; Jiang, H.; Brouwer, F.M. Geochemistry and zircon U-Pb-Hf isotopes of Paleozoic granitoids along the Solonker suture zone in Inner Mongolia, China: Constraints on bidirectional subduction and closure timing of the Paleo-Asian Ocean. *Gondwana Res.* **2024**, *126*, 1–21. [CrossRef]
7. Zonenshaĭn, L.P.; Kuzmin, M.I.; Natapov, L.M. Geology of the USSR: A plate-tectonic synthesis. *Pure Appl. Geophys.* **1990**, *140*, 120.
8. Eizenhöfer, P.R.; Zhao, G.C.; Zhang, J.; Sun, M. Final closure of the Paleo-Asian Ocean along the Solonker Suture Zone: Constraints from geochronological and geochemical data of Permian volcanic and sedimentary rocks. *Tectonics* **2014**, *33*, 441–463. [CrossRef]
9. Guo, F.; Li, H.X.; Fan, W.M.; Li, J.Y.; Zhao, L.; Huang, M.W.; Xu, W.L. Early Jurassic subduction of the Paleo-Pacific Ocean in NE China: Petrologic and geochemical evidence from the Tumen mafic intrusive complex. *Lithos* **2015**, *224–225*, 46–60. [CrossRef]
10. Li, S.Z.; Suo, Y.H.; Li, X.Y.; Zhou, J.; Santosh, M.; Wang, P.C.; Wang, G.Z.; Guo, L.L.; Yu, S.Y.; Lan, H.Y.; et al. Mesozoic tectono-magmatic response in the East Asian ocean-continent connection zone to subduction of the Paleo-Pacific Plate. *Earth Sci. Rev.* **2019**, *192*, 91–137. [CrossRef]
11. Teng, G.; Liu, S.W.; Wang, M.J.; Bao, H. Petrogenesis and tectonic implications of the Mesozoic granitoid intrusions in the eastern Liaoning Peninsula, NE China. *J. Asian Earth Sci.* **2020**, *195*, 104356. [CrossRef]
12. Zhang, T.; Qiu, H.N.; Wu, Y.; Zhang, D.H. Petrogenesis of Middle Jurassic mafic dikes and granites in the eastern Hebei district, North China Craton, China: Implications for westward subduction of the Paleo-Pacific plate. *J. Asian Earth Sci.* **2024**, *272*, 106248. [CrossRef]
13. Li, D.P.; Jin, Y.; Hou, K.J.; Chen, Y.L.; Lu, Z. Late Paleozoic final closure of the Paleo-Asian Ocean in the eastern part of the Xing-Meng Orogenic Belt: Constraints from Carboniferous-Permian (meta-) sedimentary strata and (meta-) igneous rocks. *Tectonophysics* **2015**, *665*, 251–262. [CrossRef]
14. Zhai, M.G.; Zhu, R.X.; Liu, J.M.; Meng, Q.R.; Hou, Q.L.; Hu, S.B.; Liu, W.; Li, Z.; Zhang, H.F.; Zhang, H.F. Time range of Mesozoic tectonic regime inversion in eastern North China Block. *Sci. China Ser. D* **2003**, *33*, 913–920. [CrossRef]
15. Davis, G.A.; Zheng, Y.D.; Wang, C.; Darby, B.J.; Zhang, C.H.; Gehrels, G. Mesozoic tectonic evolution of the Yanshan fold and thrust belt with emphasis on Hebei and Liaoning Provinces, northern China. *Beijing Geol.* **2002**, *10*, 171–197. (In Chinese with English Abstract)
16. Cai, J.H.; Yan, G.H.; Mu, B.L.; Ren, K.X.; Song, B.; Li, F.T. Zircon U-Pb age, Sr-Nd-Pb isotopic compositions and trace element of Fangshan complex in Beijing and their petrogenesis significance. *Acta Petrol. Sin.* **2005**, *21*, 776–788.
17. Fan, W.M.; Zhang, H.F.; Baker, J.; Javis, K.E.; Mason, P.R.D.; Menzies, M.A. On and off the North China Craton: Where is the Archean keel. *J. Petrol.* **2000**, *41*, 933–950. [CrossRef]
18. Gao, S.; Rudnik, R.L.; Yuan, H.L.; Liu, X.M.; Liu, Y.S.; Xu, W.L.; Ling, W.L.; Ayers, J.; Wang, X.C.; Wang, Q.H. Recycling lower continental crust in the North China Craton. *Nature* **2004**, *432*, 892–897. [CrossRef]
19. Shao, J.A.; Mu, B.L.; Zhang, Y.Q. Deep geological process and its shallow response during Mesozoic transfer of tectonic frameworks in eastern North China. *Geol. Rev.* **2000**, *46*, 32–39. (In Chinese with English Abstract)
20. Zhang, S.H.; Zhao, Y.; Davis, G.A.; Ye, H.; Wu, F. Temporal and spatial variations of Mesozoic magmatism and deformation in the North China Craton: Implications for lithospheric thinning and decratonization. *Earth Sci. Rev.* **2014**, *131*, 49–87. [CrossRef]
21. Zhang, S.H.; Zhao, Y. Cogenetic origin of mafic microgranular enclaves in calc-alkaline granitoids: The Permian plutons in the northern North China Block. *Geosphere* **2017**, *13*, 482–517. [CrossRef]
22. Ying, J.F.; Zhang, H.F.; Tang, Y.J. Crust-mantle interaction in the central North China Craton during the Mesozoic: Evidence from zircon U-Pb chronology, Hf isotope and geochemistry of syenitic-monzonitic intrusions from Shanxi province. *Lithos* **2011**, *125*, 449–462. [CrossRef]

23. Ma, X.Y. *Atlas of Active Fault of China*; Seismologic Press: Beijing, China, 1989; p. 120.

24. Ying, J.F.; Zhang, H.F.; Sun, M.; Tang, Y.J.; Zhou, X.H.; Liu, X.M. Petrology and geochemistry of Zijinshan alkaline intrusive complex in Shanxi Province, western North China Craton: Implication for magma mixing of different sources in an extensional regime. *Lithos* **2007**, *98*, 45–66. [CrossRef]

25. Zhao, G.C.; Sun, M.; Wilde, S.A.; Li, S.Z. Late Archean to Paleoproterozoic evolution of the North China Craton: Key issues revisited. *Precambrian Res.* **2005**, *136*, 177–202. [CrossRef]

26. Su, Y.P.; Zheng, J.P.; Griffin, W.L.; Zhao, J.H.; Li, Y.L.; Wei, Y.; Huang, Y. Zircon U-Pb ages and Hf isotope of gneissic rocks from the Huai'an Complex: Implications for crustal accretion and tectonic evolution in the northern margin of the North China Craton. *Precambrian Res.* **2014**, *255*, 335–354. [CrossRef]

27. Shao, J.A.; Zhang, Y.B.; Zhang, L.Q.; Mu, B.L.; Wang, P.Y.; Guo, F. Early Mesozoic dike swarms of carbonatites and lamprophyres in Datong ares. *Acta Petrol. Sin.* **2003**, *19*, 93–104. (In Chinese with English Abstract)

28. Zhang, H.F.; Wang, H.Z.; Santosh, M.; Zhai, M.G. Zircon U-Pb ages of Paleoproterozoic mafic granulites from the Huai'an terrane, North China Craton (NCC): Implications for timing of cratonization. *Precambrian Res.* **2016**, *272*, 244–263. [CrossRef]

29. Santosh, M.; Liu, S.J.; Tsunogae, T.; Li, J.H. Paleoproterozoic ultrahigh-temperature granulites in the North China Craton: Implications for tectonic models on extreme crustal metamorphism. *Precambrian Res.* **2012**, *222–223*, 77–106. [CrossRef]

30. Yang, Q.Y.; Santosh, M. Charnockite magmatism during a transitional phase: Implications for Late Paleoproterozoic ridge subduction in the North China Craton. *Precambrian Res.* **2015**, *261*, 188–216. [CrossRef]

31. Ma, X.D.; Guo, J.H.; Liu, F.; Qian, Q.; Fan, H.R. Zircon U-Pb ages, trace elements and Nd-Hf isotopic geochemistry of Guyang sanukitoids and related rocks: Implications for the Archean crustal evolution of the Yinshan Block, North China Craton. *Precambrian Res.* **2013**, *230*, 61–78. [CrossRef]

32. Ma, X.D.; Fan, H.R.; Santosh, M.; Guo, J.H. Petrology and geochemistry of the Guyang hornblendite complex in the Yinshan block, North China Craton: Implications for the melting of subduction-modified mantle. *Precambrian Res.* **2016**, *273*, 38–52. [CrossRef]

33. Liu, J.J.; Ye, L.; Niu, Y.L.; Guo, P.Y.; Sun, P.; Cui, H.X. The Geochemistry of Late Mesozoic Volcanic Rocks From the North China Craton and Temporal and Spatial Constraints on the Lithospheric Thinning. *Geol. J. China Univ.* **2014**, *4*, 491–506. (In Chinese with English Abstract)

34. Qiao, H.Z.; Yin, C.Q.; Li, Q.L.; He, X.L.; Qian, J.H.; Li, W.J. Application of the revised Ti-in-zircon thermometer and SIMS zircon U-Pb dating of high-pressure pelitic granulites from the Qianlishan-Helanshan Complex of the Khondalite Belt, North China Craton. *Precambrian Res.* **2016**, *276*, 1–13. [CrossRef]

35. Chen, C.; Zhang, Z.C.; Li, K.; Chen, Y.; Tang, W.H.; Li, J.F. Geochronology, geochemistry, and its geological significance of the Damaoqi Permian volcanic sequences on the northern margin of the North China Block. *J. Asian Earth Sci.* **2015**, *97*, 307–319. [CrossRef]

36. Tong, Y.; Jahn, B.M.; Wang, T.; Hong, D.W.; Smith, E.I.; Sun, M.; Gao, J.F.; Yang, Q.D.; Huang, W. Permian alkaline granites in the Erenhot-Hegenshan belt, northern Inner Mongolia, China: Model of generation, time of emplacement and regional tectonic significance. *J. Asian Earth Sci.* **2015**, *97*, 320–336. [CrossRef]

37. Niu, Y.L. Generation and evolution of basaltic magmas: Some basic concepts and a new view on the origin of Mesozoic-Cenozoic basaltic volcanism in eastern China. *Geol. J. China Univ.* **2005**, *11*, 9–46. (In Chinese with English Abstract)

38. Wang, J.; Wu, Y.B.; Gao, S.; Peng, M.; Liu, X.C.; Zhao, L.S.; Zhou, L.; Hu, Z.C.; Gong, H.J.; Liu, Y.S. Zircon U-Pb and trace element data from rocks of the Huai'an Complex: New insights into the late Paleoproterozoic collision between the Eastern and Western Blocks of the North China Craton. *Precambrian Res.* **2010**, *178*, 59–71. [CrossRef]

39. Wu, J.L.; Zhang, H.F.; Zhai, M.G.; Guo, J.H.; Liu, L.; Yang, W.Q.; Wang, H.Z.; Zhao, L.; Jia, X.L.; Wang, W. Discovery of pelitic high-pressure granulite from Manjinggou of the Huai'an Complex, North China Craton: Metamorphic P-T evolution and geological implications. *Precambrian Res.* **2016**, *278*, 323–336. [CrossRef]

40. Mu, B.L.; Yan, G.H. Geochemistry of Triassic alkaline or subalkaline igneous complexes in the Yan-Liao area and their significance. *Acta Geol. Sin.* **1992**, *66*, 108–121. (In Chinese with English Abstract)

41. Black, L.P.; Kamo, S.L.; Allen, C.M.; Aleinikoff, J.N.; Davis, D.W.; Korsch, R.J.; Foudoulis, C. TEMORA 1: A new zircon standard for Phanerozoic U–Pb geochronology. *Chem. Geol.* **2003**, *200*, 155–170. [CrossRef]

42. Wan, Y.S.; Song, B.; Liu, D.Y.; Wilde, S.A.; Wu, J.S.; Shi, Y.R.; Yin, X.Y.; Zhou, H.Y. SHRIMP U-Pb zircon geochronology of Palaeoproterozoic metasedimentary rocks in the North China Craton: Evidence for a major Late Palaeoproterozoic tectonothermal event. *Precambrian Res.* **2006**, *149*, 249–271. [CrossRef]

43. Ludwig, K.R. *Isoplot/Ex Version 4: A Geochronological Toolkit for Microsoft Excel*; Geochronology Center: Berkeley, CA, USA, 2011; p. 74.

44. Yang, Y.H.; Zhang, H.F.; Chu, Z.Y.; Xie, L.W.; Wu, F.Y. Combined chemical separation of Lu, Hf, Rb, Sr, Sm and Nd from a single rock digest and precise and accurate isotope determinations of Lu-Hf, Rb-Sr and Sm-Nd isotope systems using Multi-Collector ICP-MS and TIMS. *Int. J. Mass Spectrom.* **2010**, *290*, 120–126. [CrossRef]

45. Middlemost, E.A.K. Naming materials in the magma/igneous rock system. *Earth Sci. Rev.* **1994**, *37*, 215–224. [CrossRef]

46. Roberts, M.P.; Clemens, J.D. Origin of high-potassium, calc-alkaline, I-type granitoids. *Geology* **1993**, *21*, 825–828. [CrossRef]

47. Sun, S.S.; McDonough, W.F. Chemical and isotopic systematics of oceanic basalts: Implications for mantle composition and processes. *Geol. Soc. Lond. Spec. Publ.* **1989**, *42*, 313–345. [CrossRef]

48. Wolf, M.B.; Wyllie, P.J. Dehydration-melting of amphibolite at 10 kbar: The effects of temperature and time. *Contrib. Mineral. Petr.* **1994**, *115*, 369–383. [CrossRef]

49. Rapp, R.P.; Watson, E.B. Dehydration melting of metabasalt at 8–32 kbar: Implications for continental growth and crust-mantle recycling. *J. Petrol.* **1995**, *36*, 891–931. [CrossRef]

50. Springer, W.; Seck, H.A. Partial fusion of basic granulites at 5 to 15 kbar: Implications for the origin of TTG magmas. *Contrib. Mineral. Petr.* **1997**, *127*, 30–45. [CrossRef]

51. Steiger, R.H.; Jäger, E. Subcommission on geochronology: Convention on the use of decay constants in geo-and cosmochronology. *Earth Planet. Sci. Lett.* **1977**, *36*, 359–362. [CrossRef]

52. Lugmair, G.W.; Marti, K. *Lunar initial* ^{143}Nd/^{144}Nd: Differential evolution of the lunar crust and mantle. *Earth Planet. Sci. Lett.* **1978**, *39*, 349–357. [CrossRef]

53. Yin, J.Y.; Yuan, C.; Sun, M.; Long, X.P.; Zhao, G.C.; Wong, K.P.; Geng, H.Y.; Cai, K.D. Late Carboniferous high-Mg dioritic dikes in Western Junggar, NW China: Geochemical features, petrogenesis and tectonic implications. *Gondwana Res.* **2010**, *17*, 145–152. [CrossRef]

54. Schiano, P.; Monzier, M.; Eissen, J.P.; Martin, H.; Koga, K.T. Simple mixing as the major control of the evolution of volcanic suites in the Ecuadorian Andes. *Contrib. Mineral. Petr.* **2010**, *160*, 297–312. [CrossRef]

55. Zhu, Y.S.; Yang, J.H.; Sun, J.F.; Zhang, J.H.; Wu, F.Y. Petrogenesis of coeval silica-saturated and silica-undersaturated alkaline rocks: Mineralogical and geochemical evidence from the Saima alkaline complex, NE China. *J. Asian Earth Sci.* **2016**, *117*, 184–207. [CrossRef]

56. Chappell, B.W.; White, A.J.R. Two contrasting granite types: 25 years later. *Aust. J. Earth Sci.* **2001**, *48*, 489–499. [CrossRef]

57. Liu, S.; Hu, R.Z.; Gao, S.; Feng, C.X.; Yu, B.B.; Feng, G.Y.; Qi, Y.Q.; Wang, T.; Coulson, I.M. Petrogenesis of Late Mesozoic Mafic Dykes in the Jiaodong Peninsula, Eastern North China Craton and Implications for The Foundering of Lower Crust. *Lithos* **2009**, *113*, 621–639. [CrossRef]

58. Yang, J.H.; Wu, F.Y.; Wilde, S.A.; Liu, X.M. Petrogenesis of Late Triassic granitoids and their enclaves with implications for post-collisional lithospheric thinning of the Liaodong Peninsula, North China Craton. *Chem. Geol.* **2007**, *242*, 155–175. [CrossRef]

59. Jelínek, E.; Dudek, A. Geochemistry of subsurface Precambrian plutonic rocks from the Brunovistulian complex in the Bohemian massif, Czechoslovakia. *Precambrian Res.* **1993**, *62*, 103–125. [CrossRef]

60. Wang, H.; Xiao, W.J.; Li, R.; Chen, H.X.; Tan, Z.; Mao, Q.G.; Shi, M.Y. High-grade complexes record the Late Permian-Middle Triassic arc metamorphism in the southernmost Altaids: Implications for the final closure of the Paleo-Asian Ocean. *Lithos* **2023**, *442–443*, 107054. [CrossRef]

61. Song, D.F.; Xiao, W.J.; Ao, S.J.; Mao, Q.G.; Wan, B.; Zeng, H. Contemporaneous closure of the Paleo-Asian Ocean in the Middle-Late Triassic: A synthesis of new evidence and tectonic implications for the final assembly of Pangea. *Earth Sci. Rev.* **2024**, *253*, 104771. [CrossRef]

62. Zhang, L.Y.; Chen, Q.; Huang, F.; Xu, J.F.; Liu, X.J.; Zhang, Z.; Zeng, Y.C.; Yang, X.L.; Zhang, Y.T.; Zhang, M.; et al. Triassic volcanism on the North margin of the North China Craton: Insights for lithospheric modification during closure of Paleo-Asian Ocean. *Lithos* **2022**, *434–435*, 106918. [CrossRef]

63. Wang, C.Y.; Liu, Y.S.; Foley, S.F.; Zong, K.Q.; Hu, Z.C. Lithospheric transformation of the northern North China Craton by changing subduction style of the Paleo-Asian oceanic plate: Constraints from peridotite and pyroxenite xenoliths in the Yangyuan basalts. *Lithos* **2019**, *328*, 58–68. [CrossRef]

64. Wang, Y.; Zhou, L.Y.; Zhao, L.J. Cratonic reactivation and orogeny: An example from the northern margin of the North China Craton. *Gondwana Res.* **2013**, *24*, 1203–1222. [CrossRef]

65. Liu, S.F. The coupling mechanism of basin and orogen in the western Ordos Basin and adjacent regions of China. *J. Asian Earth Sci.* **1998**, *16*, 369–383. [CrossRef]

66. Pearce, J.A.; Harris, N.B.W.; Tindle, A.G. Trace Element Discrimination Diagrams for the Tectonic Interpretation of Granitic Rocks. *J. Petrol.* **1984**, *25*, 956–983. [CrossRef]

67. Dong, S.W.; Zhang, Y.Q.; Long, C.X.; Yang, Z.Y.; Ji, Q.; Wang, T.; Hu, J.M.; Chen, X.H. Jurassic tectonic revolution in China and new interpretation of the 'Yanshan Movement'. *Acta Petrol. Sin.* **2007**, *82*, 334–347. (In Chinese with English Abstract)

68. Dong, S.W.; Zhang, Y.Q.; Cheng, X.H.; Long, C.Q.; Wang, T.; Yang, Z.Y.; Hu, J.M. The formation and deformational characteristics of East Asia multi-direction convergent tectonic system in Late Jurassic. *Acta Petrol. Sin.* **2008**, *29*, 306–317. (In Chinese with English Abstract)

69. Wang, T.; Guo, L.; Zhang, L.; Yang, Q.D.; Zhang, J.J.; Tong, Y.; Ye, K. Timing and evolution of Jurassic-Cretaceous granitoid magmatisms in the Mongol-Okhotsk belt and adjacent areas, NE Asia: Implications for transition from contractional crustal thickening to extensional thinning and geodynamic settings. *J. Asian Earth Sci.* **2015**, *97*, 365–392. [CrossRef]

70. Ge, L.S.; Wang, Z.H.; Yang, G.C.; Lu, Y.C. Yanshanian magmatism and gold-polymetallic mineralization dynamics in northeastern Shanxi Province, China. *Acta Petrol. Sin.* **2012**, *28*, 619–636.

71. Qiang, R.; Zhang, S.H.; Wu, H.C.; Liang, Z.K.; Miao, X.J.; Zhao, H.Q.; Li, H.Y.; Yang, T.S.; Pei, J.L.; Davis, G.A. Further paleomagnetic results from the ~155 Ma Tiaojishan Formation, Yanshan Belt, North China, and their implications for the tectonic evolution of the Mongol-Okhotsk suture. *Gondwana Res.* **2016**, *35*, 180–191.

72. Zhao, Y.; Chen, B.; Zhang, S.H.; Liu, J.M.; Hu, J.M.; Liu, J.; Pei, J.L. Pre-Yanshanian geological events in the northern margin of the North China Craton and its adjacent areas. *Geol. China* **2010**, *37*, 900–915.

73. Tang, J.; Xu, W.L.; Wang, F.; Ge, W.C. Subduction history of the Paleo-Pacific slab beneath Eurasian continent: Mesozoic-Paleogene magmatic records in Northeast Asia. *Sci. China Earth Sci.* **2018**, *61*, 527–559. [CrossRef]

74. Guo, J.F.; Ma, Q.; Xu, Y.G.; Zheng, J.P.; Zou, Z.Y.; Ma, L.; Bai, X.J. Migration of Middle-Late Jurassic volcanism across the northern North China Craton in response to subduction of Paleo-Pacific Plate. *Tectonophysics* **2022**, *833*, 229338. [CrossRef]

75. Li, Y.; Xu, W.L.; Tang, J.; Pei, F.P.; Wang, F.; Sun, C.Y. Geochronology and geochemistry of Mesozoic intrusive rocks in the Xing'an Massif of NE China: Implications for the evolution and spatial extent of the Mongol-Okhotsk tectonic regime. *Lithos* **2018**, *304*, 57–73. [CrossRef]

76. Li, Y.; Xu, W.L.; Zhang, X.M.; Tang, J. Late Mesozoic stratigraphic framework of the Great Xing'an Range, NE China, and overprinting by the Mongol-Okhotsk and Paleo-Pacific tectonic regimes. *Gondwana Res.* **2024**, *134*, 91–106. [CrossRef]

77. Li, Z.H.; Qu, H.J.; Gong, W.B. Late Mesozoic basin development and tectonic setting of the northern North China Craton. *J. Asian Earth Sci.* **2015**, *114*, 115–139. [CrossRef]